Sensor and Simulation Notes

Note 584

May 14, 2022

Improved image processing for electromagnetic infrared thermography

Tobias Baumgartner[a] and Daniel Prost[b]

[a]*Technical University of Munich, Munich, Germany,*

[b]*ONERA/DEMR, Université de Toulouse, F-31055 Toulouse, France.*

Email: tobi.baumgartner@tum.de, daniel.prost@onera.fr

Abstract

In the 1980s, an electromagnetic infrared method was initially developed at the US Air Force Academy (USAFA) and the University of Colorado at Colorado Springs (UCCS) that produced the first images of EM fields made by an Infrared camera measuring the heating of absorbing materials. In the 1990s, this field imaging method was then enhanced by the French Aerospace Lab ONERA, under the registered name "EMIR", as an electric field measurement technique by introducing synchronous modulation of the EM incident signal. EMIR provides two-dimensional representations of the electric field, through a quasi-instantaneous measurement. This can be useful for fast characterization of radiating sources, especially in the microwave frequency range. In addition, it is capable of imaging subwavelength details.

In this paper, a digital signal processing scheme is proposed that consists of applying a temporal and spatial filtering to the video signal. Considering the trade-off between additive noise, uncertainty over system parameters and optical transfer, the signal-to-noise ratio can be improved by up to 8 dB. Further, the advantages of a chirp modulation signal over a single frequency lock-in thermography system is demonstrated.

1. **Introduction**

Characterizing electromagnetic (EM) fields emitted by various sources is an important issue, either for civil or military applications (telecommunications, radar, antennas, civil and military aeronautics, medicine, etc.). With a single probe, a local EM field measurement can be performed, but for the visualization of a spatial distribution a stepwise displacement of the probe is necessary, which can be time-consuming. Consequently, infrared thermography is an alternative way that provides a field map in reduced time. This method was developed in the early nineties [1, 2] and is used at ONERA where we call it EMIR (ElectroMagnetic InfraRed) [3]. It aims to obtain a visualization, and a quantitative measurement through calibration, of the electric field amplitude radiated by the microwave source under test. The EMIR method consists in irradiating a weakly conductive thin film to the EM field. The induced currents cause the film to heat up in proportion to the power absorbed, which is then recorded by the infrared camera (Figure 1). In order to increase the spatial resolution, and eliminate continuous thermal phenomena (convection, conduction), the EM source is modulated at a low frequency f (= some few Hz), and the series of image frames is demodulated at the same frequency.

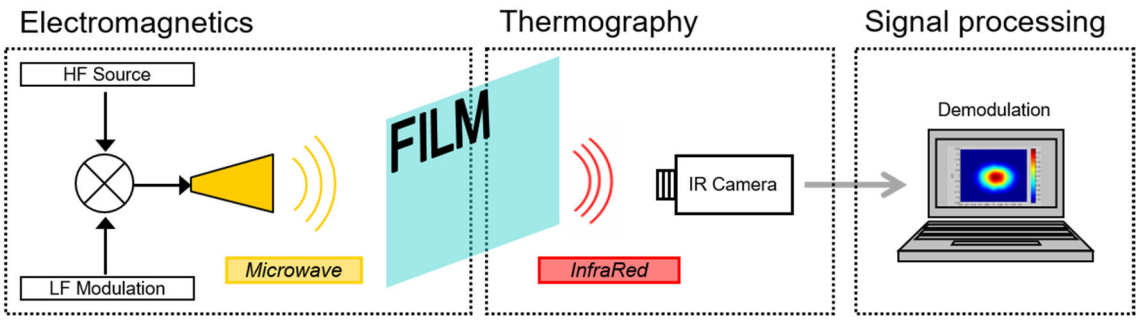

Figure 1. EMIR method: the thin film absorbs a portion of the radiated energy and heats up, which is detected by the thermal camera; the video is then digitally demodulated.

Previously, the demodulation of the lock-in thermography was carried out by an analogue circuit board that was associated with the camera and the reference signal generator. Each pixel of the recorded video signal was multiplied with the sinusoidal modulation signal and a 90-degree shifted version of it. The resulting in-phase and quadrature components were then accumulated into two image buffers [2]. These could then be converted into an amplitude and a phase image, the former being proportional to the EM absorbed power. Since only the output images were available, the user had no control over the signal processing, which presents a drawback of such an analogue lock-in thermography system.

However, in the case where all the recorded frames are available (no buffering), it becomes obvious that Digital Signal Processing (DSP) could be used to improve the demodulation process. A

single data acquisition usually consists of hundreds or thousands of infrared frames. Considering a typical high-performance camera with 640x512 pixels sensor (like the one we use [4]), there is an order of magnitude of 1 GB (for a typical recording of 1000 frames) of data to process. A standard personal computer can handle this amount of data.

The objective of this paper is to demonstrate that DSP techniques to extract the power density distribution from a thermal video signal. After an analysis of the measurement chain in section 2, we present in section 3 different filtering approaches, from elementary to more complicated schemes; we illustrate in section 4 how they improve the dynamic range of the image by enhancing the signal-to-noise ratio (SNR).

2. **Acquisition model**

Previous works have optimized the EMIR method with respect to certain sub parts of the imaging system [5]. In doing so, the thin film (especially its material and thickness), the camera (noise and framerate), and the modulation process (frequency) were considered individually.

However, no optimization process has yet considered the entire system as a whole from a signal processing point of view. Therefore, we present here a model of the entire signal chain that associates the sub parts of the system, which are the radiation system [resulting in a power density p –modulated by a function g- on the location (x,y) of the film], the thin film (with optical transfer function M that depends on the modulation frequency f of the g modulation signal, and on spatial variations of the heating on the film at spatial frequencies f_x, f_y), the thermal camera (that adds a noise n), and the filter H. This signal chain is shown in Figure 2.

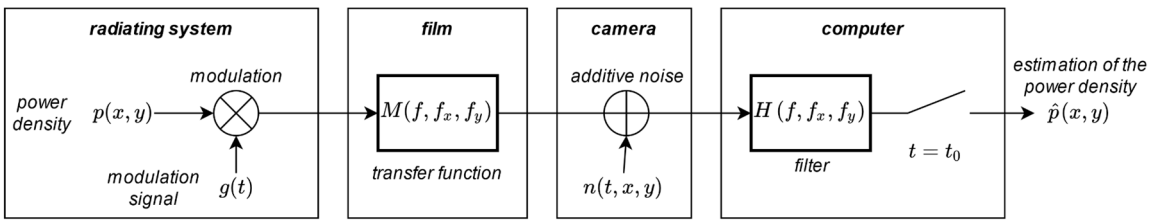

Figure 2. Signal chain.

2.1. Signal chain

The EMIR method is an imaging system, which is equivalent to making an image (2D map of the magnitude of the electric field) from a scene (EM power density). Let us say $p(x,y)$ is a 2D cut of the 3D power distribution that we intend to map. The output of the imaging system, as a 2D signal, is then an estimate $\hat{p}(x,y)$ of the real image $p(x,y)$. The process of modulating the power source is

solely an intermediate step of the imaging process since the dimension of time is eliminated after the filtering step.

First, the real image $p(x, y)$ is modulated with the signal $g(t)$, which corresponds to the squared amplitude of the output of the signal generator. The resulting tri-dimensional signal *p(t,x,y)* is then transformed by the thin film into a temperature video signal $\tau(t, x, y)$. This transformation is a linear shift-invariant system (see paragraph 2.3) with the impulse response $m(t, x, y)$. During sampling with the camera, the signal is disturbed by noisy phenomena, that we model with an additive noise $n(t, x, y)$. The resulting video signal is then digitally processed by a filter operation with an impulse response $\hbar(t, x, y)$ and finally the signal is sampled in time at $t = t_0$ to obtain an image.

We can, therefore, relate the estimated image $\hat{p}$ and the real image p through the following equation:

$$\hat{p}(x, y) = [(p \cdot g) * m * \hbar]\,(t_0, x, y) + (n * \hbar)(t_0, x, y) \tag{1}$$

where $*$ denotes the three-dimensional convolution.

2.2. Optical transfer function

With the Fourier transform we can also write:

$$\begin{aligned}\hat{p}(x, y) = {} & (n * \hbar)(t_0, x, y) \\ & + \iint P(f_x, f_y) \int G(f) M(f, f_x, f_y) H(f, f_x, f_y) e^{i2\pi f t_0} df\, e^{i2\pi f_x x} e^{i2\pi f_y y}\, df_x df_y\end{aligned} \tag{2}$$

where the uppercase letters stand for the Fourier transform of the according lowercase letters (H corresponds to $\hbar$ (letter with a bar) since the letter h (without a bar) is the heat transfer coefficient). By neglecting the noise for the instance, we can write the image spectrum of $\hat{p}$ as a simple product:

$$\hat{P}(f_x, f_y) = P(f_x, f_y)\, OTF(f_x, f_y) \tag{3}$$

where "OTF " is the optical transfer function:

$$\mathrm{OTF}(f_x, f_y) = \int G(f) M(f, f_x, f_y) H(f, f_x, f_y) e^{i2\pi f t_0} df \tag{4}$$

The inverse Fourier transform of the optical transfer function is the point spread function $\mathrm{PSF}(x, y) = \mathcal{F}^{-1}_{x,y}\{\mathrm{OTF}(f_x, f_y)\}$ [6], which will be noted “PSF”. The goal is that the estimated image is as close as possible to the real image:

$$\hat{P}(f_x, f_y) \approx P(f_x, f_y) \tag{5}$$

Thus, we want to design our system such that $otf(f_x, f_y) \approx 1$ for the spatial frequencies f_x and f_y of interest. For this, we need to choose a modulation signal G and a filter H well adapted to the transfer function M of the film. One might propose to set the filter H as the inverse of M. However, we also need to consider the influence of the noise (section 3). But first, we characterize the transfer function M.

2.3. Thin film transfer function

The heat equation in the thin film is given by:

$$\rho C_p \frac{\partial T(t,\vec{r})}{\partial t} - \kappa \Delta T(t,\vec{r}) = G(t,\vec{r}) \tag{6}$$

where ρ is the film density, C_p its specific heat capacity of the film, and κ the thermal conductivity of the film. The power density $G(r,t)$ corresponds to the net rate at which energy is generated in the film. This is the EM absorbed power density p_v minus the heat convection and radiation as the film loses energy to the ambient room. As the Biot number $B_i = h.d/\kappa$ (where d is the film thickness) is much smaller than 1 (see below) we can assume identical temperatures on both sides of the film. Moreover, if the temperature variation is small compared to the ambient temperature T_0, the radiation and convection terms can be linearized into a single modified heat transfer coefficient h [7]. The equation becomes:

$$\rho C_p \frac{\partial T(t,\vec{r})}{\partial t} - \kappa \Delta T(t,\vec{r}) = p_v(t,\vec{r}) - 2h[T(t,\vec{r}) - T_0]/d \tag{7}$$

Under the assumption of the "lumped system formulation" [7] (since $\rho = 1420\ kgm^{-3}$, $C_p = 1090\ Jkg^{-1}K^{-1}$, $\kappa = 0.5\ WK^{-1}m^{-1}$, $h = 15\ WK^{-1}m^{-2}$, film thickness $d = 50\ \mu m$, the Biot number $B_i < 0.001$ is much smaller than 1 and the thermal diffusion length [8], $L_t = \sqrt{\frac{\kappa}{\rho C_p 2\pi f}} > 0.1\ mm$, is large compared to the film thickness), the temperature is constant over the film thickness. The films we use are typically made of carbon loaded Kapton with a conductivity in the range of 5 to 20 Sm^{-1}. Since the skin depth is large compared to the film thickness ($d = 50\ \mu m$), the absorbed power is uniform in the thickness of the film.

Under these assumptions, the heat equation can be written as a function of two spatial dimensions only. The pertinent power entity is now the *surface* power density $p(t,x,y)$ and we have

$$\rho C_p d \frac{\partial T(t,x,y)}{\partial t} - \kappa d \frac{\partial^2 T(t,x,y)}{\partial x^2} - \kappa d \frac{\partial^2 T(t,x,y)}{\partial y^2} = p(t,x,y) - 2h[T(t,x,y) - T_0] \quad (8)$$

By applying the Fourier transform with respect to t, x and y, we can derive the transfer function M of the film, which transforms an EM surface power to a temperature signal:

$$M(f, f_x, f_y) = \frac{1}{2h + \kappa d 4\pi^2 ({f_x}^2 + {f_y}^2) + i\rho C_p d 2\pi f} \quad (9)$$

This function is tri-dimensional, but it has a radial symmetry. We can thus introduce the polar frequency $f_r = \sqrt{(f_x^2 + f_y^2)}$. Figure 3 shows the modulus of $M(f, f_r)$ for carbon loaded Kapton and the iso-f lines (for integer multiples of a typical modulation frequency $f = f_m = 0.5$ Hz):

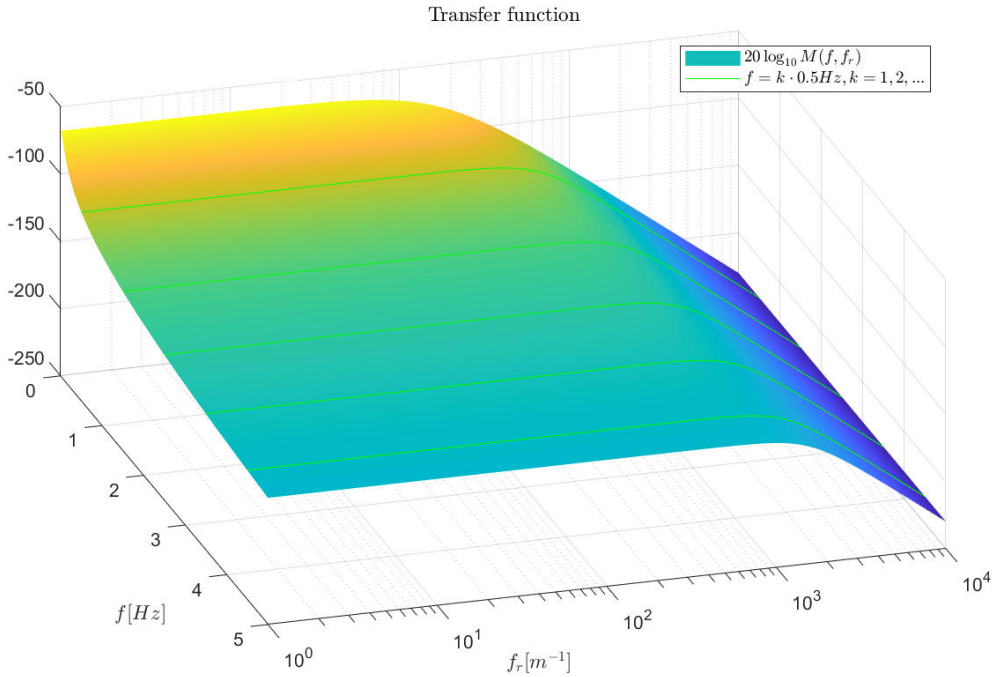

Figure 3. Film transfer function $M(f, f_r)$ on a logarithmic scale in the f_r direction, on a linear scale in f direction.

3. **Filtering approaches**

Several filtering approaches are considered.

3.1. In-phase demodulation

The video recording containing all the frames is processed after the measurement. By multiplying the time signal of each pixel by a complex exponential at the modulation frequency f, i.e., $\hbar(t) = e^{j2\pi f t}$, as it was achieved by the analogic circuit board, the optical transfer function can be expressed as:

$$\mathrm{OTF}(f_r) = \frac{c\, e^{-j2\pi f \Delta t}}{2h + \kappa d 4\pi^2 {f_r}^2 + i\rho C_p d 2\pi f} \tag{10}$$

with a normalization constant c and the time shift Δt between the modulation and the demodulation signal. Because of the radial symmetry, we can calculate the PSF by using the zero-order Hankel transform [9]. It can then be expressed with the modified Bessel zero-order function K_0 [10], which is depicted in Figure 4:

$$\mathrm{PSF}(r) = \frac{c e^{-j2\pi f \Delta t}}{2\pi\kappa d} K_0(\beta r) \tag{11}$$

with $r = \sqrt{x^2 + y^2}$ and $\beta = \sqrt{\frac{i\rho C_p d 2\pi f + 2h}{\kappa d}} \approx \frac{1+i}{\sqrt{2}} \frac{1}{L_t}$ (L_t is the diffusion length).

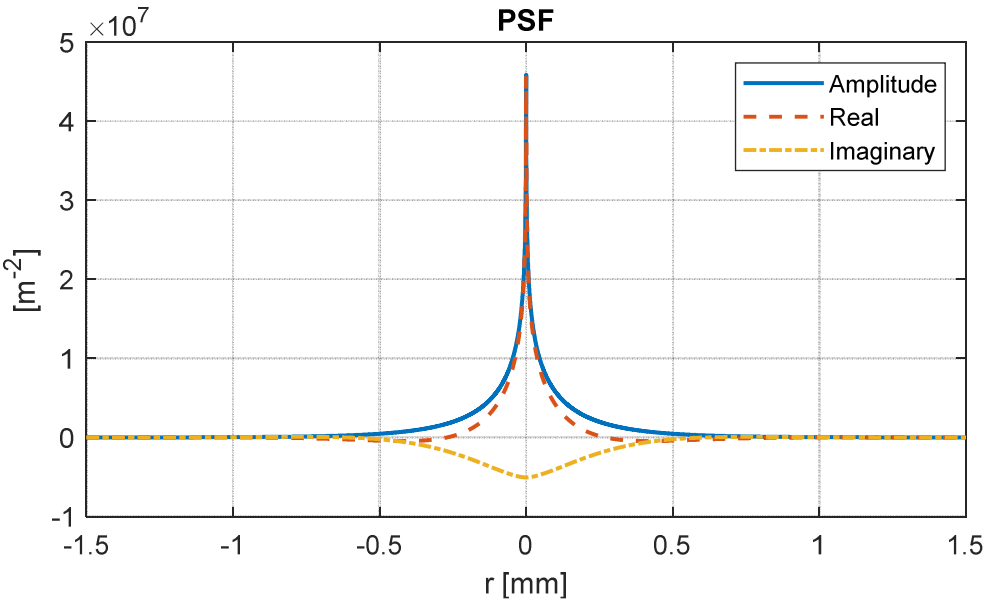

Figure 4. Point spread function when the heat energy transfer exceeds convection, i.e., $2h$ can be neglected and no time shift ($\Delta t = 0$).

We notice that the PSF is complex with the real part being better resolved than the imaginary part. Also, the real part dominates the imaginary part around zero. We can, thus, increase the resolution by taking the real part of the complex image. However, we must assure that the time shift is zero, i.e., $\mathrm{Re}\{e^{-j2\pi f \Delta t}\} = 1$. This can be achieved by *demodulating in phase*. In addition, taking the real part eliminates the imaginary part of the noise. This improves the SNR by 3 dB compared to taking the absolute value.

3.2. Spatial filtering

Through spatial filtering of the demodulated image, we can eliminate high (spatial) frequencies that are generally associated with noise. This can be done after the demodulation process, by applying different low-pass filters that truncate, or attenuate (Butterworth filter, Gaussian filter etc.) high

frequencies. However, the cut-off frequency used for these spatial filters is somewhat arbitrary. This limits the significance and, therefore, the interest in spatial filtering. A better approach is, therefore, to use the transfer function that represents the physical behavior of the thin film, to address spatial filtering. This can be done by using a spatially matched filter that maximizes the SNR:

$$H(f_r) = \frac{\overline{M(f, f_r)}}{|M(f, f_r = 0)|} \tag{12}$$

In this equation (as in the following ones), the overbar is for complex conjugate. The denominator is a normalization constant that ensures that the absorbed power does not change. This operation is a low-pass filtering with a cut off frequency of $f_r = \frac{1}{2\pi L_t}$. The PSF is now a real function and it takes the form of the Kelvin *kei* function, as it was the case with the imaginary part of the PSF in section 3.1.

Instead of spatially filtering the already demodulated image, we can design a filter that is applied in all three dimensions at once. Nevertheless, applying the spatial filter after the demodulation can be useful in the case where the video recording is not available or for the purpose of computing efficiency.

3.3. Matched filter

So far, we have demodulated the temperature signal at one frequency, i.e., the modulation frequency $f = f_m$. However, the measured signal might have a richer spectrum than the one of a purely sinusoidal signal. For instance, if a periodic on-off switch controls the microwave power source, a square wave is generated. The modulation signal and, consequently, the temperature signal then have harmonics of higher order. We can use these parts of the signal to increase the SNR. Instead of demodulating at several frequencies and then combining the resulting images, we can use a filter to extract all the useful information of the signal at once. However, if we exploit the entire spectrum of the measured signal (not only $f = f_m$, but $f \in \left[0, \frac{FPS}{2}\right]$), we must consider the transfer function $M(f, f_r)$ for all f. Consequently, it is useless to apply the spatial filter after the temporal filtering as in section 3.2. But we can develop a tri-dimensional filter $H(f, f_r)$. One way of designing H is by using the matched filter which maximizes the SNR for a single ideal image point [EM density is a 2D Dirac impulse: $p(x, y) = p_0\delta(x - x_0, y - y_0)$, with the intensity p_0]. We define the SNR as the signal power $\mathrm{S} = \hat{p}(x_0, y_0)^2$ over the additive noise power N_{add} using the Parseval's theorem and the Wiener–Khinchin theorem respectively:

$$\mathrm{SNR} = \frac{S}{N_{add}} = \frac{p_0^2 \left| \iiint G(f) M(f, f_r) H(f, f_r) e^{i2\pi f t_0} df df_x \, df_y \right|^2}{\iiint S_n(f, f_r) |H(f, f_r)|^2 df df_x \, df_y} \tag{13}$$

where S_n is the noise power density of the additive noise and with an *arbitrary* (not only a square wave) modulation signal with the spectrum $G(f)$. By maximization of the SNR, the tri-dimensional filter is then given by:

$$H(f, f_r) = \frac{\overline{G(f) M(f, f_r)}}{Z \, S_n(f, f_r)} e^{-i2\pi f t_0} \tag{14}$$

where Z is a normalization constant that assures that $\mathrm{OTF}(f_r = 0) = 1$[11]. This filter acts differently on the spatial components depending on f.

3.4. Heat coefficient influence

If f and f_r are small, then the term $2h$ corresponding to natural convection phenomena determines the transfer function [see equation (10)]. This term is in general not well known and depends on the temperature difference between the film and the ambient air as it is obtained through linearization. Values between 5 and 20 $\mathrm{WK^{-1}m^{-2}}$ are usually used as a rough estimation for h. This uncertainty can be included in the filtering process by describing h as a random variable with its probability density function. For example, we can represent h with a normal distribution : h_0 centered and with standard deviation σ_h.

We use this probabilistic approach to derive a noise power that arises from the propagation of the uncertainty over h. We define the noise power N_{otf} as the variance of the optical transfer function accumulated over the power spectral density $S_p(f_r)$ of the image $p(x, y)$:

$$N_{otf} = \iint S_p(f_r) Var[otf(f_r)] df_x \mathrm{d}f_y \tag{15}$$

where $Var[\cdot]$ denotes the variance operator with respect to the distribution of h. We remark that equation (15) can be generalized to include uncertainty over several system parameters at the same time.

As we are still considering an ideal image point, the power spectrum is uniform. i.e., $S_p(f_r) = p_0^2$. However, we note the more general form as we will reuse this result in the next section.

Through extension and rearrangement, we can write the noise power in the form of a filtered noise power density:

$$N_{otf} = \iiint S_{otf}(f, f_r) |H(f, f_r)|^2 \, df df_x df_y \tag{16}$$

The noise power density $S_{otf}(f, f_r) = S_p(f_r)U(f, f_r)$ can be written as the product of the signal power spectrum and, what we call the "uncertainty transfer function":

$$U(f, f_r) = K(f, f_r)[\frac{1}{\overline{E[M(f, f_r)]}} \int \frac{|G(f')|^2}{K(f', f_r)} \overline{E[M(f', f_r)]} E\left[M(f', f_r)\overline{M(f, f_r)}\right] df' - \int \frac{|G(f')|^2}{K(f', f_r)} |E[M(f', f_r)]|^2 df'] \tag{17}$$

with $E[\cdot]$ denoting the expected value with respect to the distribution of h. Then, we can extend the definition of the SNR:

$$SNR = \frac{S}{N_{add} + N_{otf}} \tag{18}$$

where S and N_{add} are, respectively, numerator and denominator from equation (13). Since N_{otf} has the same form as N_{add}, we can regroup the interiors of the integrals to

$$K(f, f_r) = S_n(f, f_r) + S_p(f_r)U(f, f_r) \tag{19}$$

The SNR is now under the same form as equation (13) so that we can reuse the previous result, the matched filter. We, therefore, have:

$$\mathrm{H}(f, f_r) = \frac{\overline{G(f)E[M(f, f_r)]}}{Z\, K(f, f_r)} e^{-i2\pi f t_0} \tag{20}$$

where Z is a normalization coefficient.

The expected value operator around $M(f, f_r)$ is necessary because of its probabilistic nature. The correction term $K(f, f_r)$ represents the additive noise, as before, plus a contribution due to uncertainty over h.

Since $U(f, f_r)$ depends on $\mathrm{K}(\mathrm{f}, f_r)$, the correction term is defined implicitly. Therefore, we cannot calculate the filter directly, but we can compute it iteratively starting with $\mathrm{K}(\mathrm{f}, \mathrm{f_r}) = S_n(f, f_r)$ until we reach the fixpoint.

This filter is designed such that it attenuates the signal in spectral regions of high uncertainty related to the heat transfer coefficient h; however, it also alters the PSF and may, thus, introduce artefacts to the image.

3.5. Wiener filter

Previously, we have optimized the SNR for a single image point $S_p(f_r) = p_0^2$. However, an image is constituted of a superposition of many points. Hence, it is not enough to consider the SNR,

but we must take into account the optical transfer function as mentioned in section 2.2. Therefore, we now consider the mean squared error in the frequency domain:

$$\epsilon(f_r) = E\left[\left|\hat{P}(f_r) - P(f_r)\right|^2\right] \tag{21}$$

with $E[\cdot]$ denoting the expected value with respect to the statistics of the signal $p(x, y)$. By insertion of the Fourier transform of equation (1) and using the solution of the matched filter (20) as an assumption, we can minimize $\epsilon(f_x, f_y)$ with respect to $K(f, f_r)$ by differentiation:

$$\mathrm{K}(\mathrm{f}, f_r) = \frac{\mathrm{S_n}(\mathrm{f}, f_r)}{\mathrm{S_p}(f_r)} + \mathrm{K}(f, f_r) \int \frac{|\mathrm{G}(\mathrm{f}')|^2 |\mathrm{M}(\mathrm{f}', f_r)|^2}{\mathrm{K}(\mathrm{f}', f_r)} \mathrm{df}' \tag{22}$$

This result is known as the Wiener filter [12], which can be interpreted as an *inverse filter* $W(f, f_r)$ (right summand) regulated by the reciprocal of the frequency-depending signal-to-noise ratio $\mathrm{SNR}_f(f, f_r) = \frac{S_p(f_r)}{S_n(f, f_r)}$ (left summand). As we are minimizing the squared error solely over the spatial frequencies (f_x, f_y), i.e., f excluded, the filter takes again an implicit form.

If we want to take into account the uncertainty over the heat transfer coefficient h, we can replace $S_n(f, f_r)$ with $S_n(f, f_r) + S_p(f_r)U(f, f_r)$. We then obtain an interpretable result:

$$\mathrm{K}(f, f_r) = \frac{1}{SNR_f(f, f_r)} + \mathrm{U}(f, f_r) + W(f, f_r) \tag{23}$$

which is a modification of equation (19), i.e., division by $S_p(f_r)$ and extension with $W(f, f_r)$.

We observe that the matched filter is modified through the interplay of the three terms of the correction term K. If the term W dominates, when the SNR is high and only small uncertainty prevails, we can check that $\mathrm{OTF}(f, f_r) \approx 1$. Otherwise, the modified matched filter H attenuates spectral regions of low SNR or high uncertainty related to h. We have, thus, found a compromise between optical transfer, noise reduction, and the influence of the uncertainty over the heat transfer coefficient h.

It remains to determine the quantities $S_p(f_r)$ and $S_n(f, f_r)$. The latter is the spectral noise density, which is camera specific and can be measured. High performance thermal cameras should exhibit a white noise, i.e. $S_n(f, f_r) = N_0$. The power spectral density $S_p(f_r)$ of the real image cannot be determined without making assumptions on the image, i.e., the EM power density distribution $p(x, y)$, that is to be measured. In some cases, the EM energy that is absorbed by the thin film is known (usually 20% of the incoming EM power [13]). Since the absorbed EM power is defined as $P_{abs} = \iint p(x, y)dxdy$, we can deduce by the definition of the power spectral density that:

$$S_p(f_r = 0) = \frac{P_{abs}^2}{A} \tag{24}$$

with the area A of the image. Further, we suppose that $p(x, y)$ is smooth to some degree. As it is done with natural images [14], the power spectral density is set to decrease with f_r to a power α. Additionally, we introduce the cut-off frequency f_{cut}, so that we can write:

$$S_p(f_r) \approx \frac{P_{abs}^2}{A} \frac{1}{1 + (f_r/f_{cut})^{\alpha}} \tag{25}$$

Eventually, we have reduced the filtering process to four degrees of freedom that need to be set heuristically: the expected value of the heat transfer coefficient h_0 and its standard deviation σ_h, the exponent α, and the cut-off frequency f_{cut}. However, the values of α, f_{cut} and h_0 can be approximated by matching the expected temperature spectrum to the radial average of the measured temperature spectrum.

3.6. Chirp modulation signal

In lock-in thermography it is common practice to modulate the power source by switching it on and off periodically [9] which generates a square wave of a modulation frequency f_m and associated odd harmonics. This, then, raises the question of how to choose this frequency. Suppose that we choose f_m too small such that the influence of the heat transfer coefficient is considerable. The matched filter (20) will then figuratively try to avoid this frequency and will prefer higher harmonics of the signal. However, with the predominant portion of the signal energy being concentrated on the fundamental frequency $f = f_m$, only little energy will be transferred and, thus, the SNR will be low. Similarly, if we choose f_m too high, we obtain a low SNR since the transfer function $M(f, f_r)$ decreases with f. In other words, if we set the modulation signal to have a single modulation frequency, the matched filter cannot figuratively avoid regions of high uncertainty without significantly degrading the SNR. This motivates the use of a chirp as the modulation signal, i.e., a signal that sweeps over several frequencies. [15, 16] use similar approaches to improve the temporal resolution in non-destructive evaluation through impulse compression. However, as EMIR images do not have a time dimension (modulation in time is an intermediate imaging step), we propose to use the chirp solely to increase the spectral diversity of the signal. Since a chirp is more difficult to implement, one might still prefer a square wave if the measurement conditions are well known.

Let us derive a temporal expression for a chirp. The instantaneous (time dependent) frequency of a signal is defined as the derivative of the instantaneous phase:

$$f(t) = \frac{1}{2\pi}\frac{d}{dt}\phi(t) \tag{26}$$

Further, we remark that the energy in a frequency range df of the modulation signal $g(t)$ is proportional to the time *dt* spent in that frequency range. We can thus write:

$$|G(f)|^2 \propto \frac{dt}{df} \tag{27}$$

We deduce here that a linear chirp exhibits a flat spectrum over the modulation band B. But, considering that the transfer function declines with f^2, the energy spectral density can differ significantly over the band. We can avoid this problem by requiring that the modulation signal compensates the low-pass characteristic of M:

$$|G(f)|^2|M(f, f_r = 0)|^2 = \text{ constant}, \quad \text{where } f_0 \leq f \leq f_0 + B \tag{28}$$

We can use this to rewrite equation (27):

$$\frac{dt}{df} \propto \frac{1}{|M(f, f_r = 0)|^2} \propto f^2 \tag{29}$$

where the second proportionality follows from an approximation of $M(f, f_r = 0)$ by neglecting the term $2h$. More generally, we can make the energy spectral density proportional to f^{n-1}, with a real valued and strictly positive degree n. This allows a free choice over the distribution of the energy in the spectrum, e.g., $n > 3$ more energy in the higher frequencies and $n < 3$ more energy in the lower frequencies.

We can now solve for the instantaneous phase for $t \in [0, T_m]$:

$$\phi(t) = 2\pi(f_{max}^n - f_0^n)^{\frac{1}{n}}\frac{n}{n+1}T_m\left(\frac{t}{T_m} + \frac{f_0^n}{f_{max}^n - f_0^n}\right)^{\frac{n+1}{n}} - 2\pi\frac{n}{n+1}T_m\frac{f_0^{n+1}}{(f_{max}^n - f_0^n)^{\frac{1}{n}}} \tag{30}$$

with $f_{max} = f_0 + B$ and the modulation period T_m.

Note, only the phases have been determined. Therefore, we still need to choose the signal function independent of the phase. As earlier, we propose the usage of a square wave such that:

$$g(t) = \text{rect}(\phi(t)), \text{ with } \text{rect}(\phi) = \begin{cases} 1, \text{ if } \phi \; mod \; 2\pi \leq \pi \\ 0, \text{ otherwise} \end{cases} \tag{31}$$

With degree $n = 3$, the resulting signal is a square-waved *cubic-root* chirp, which is depicted in Figure 5.

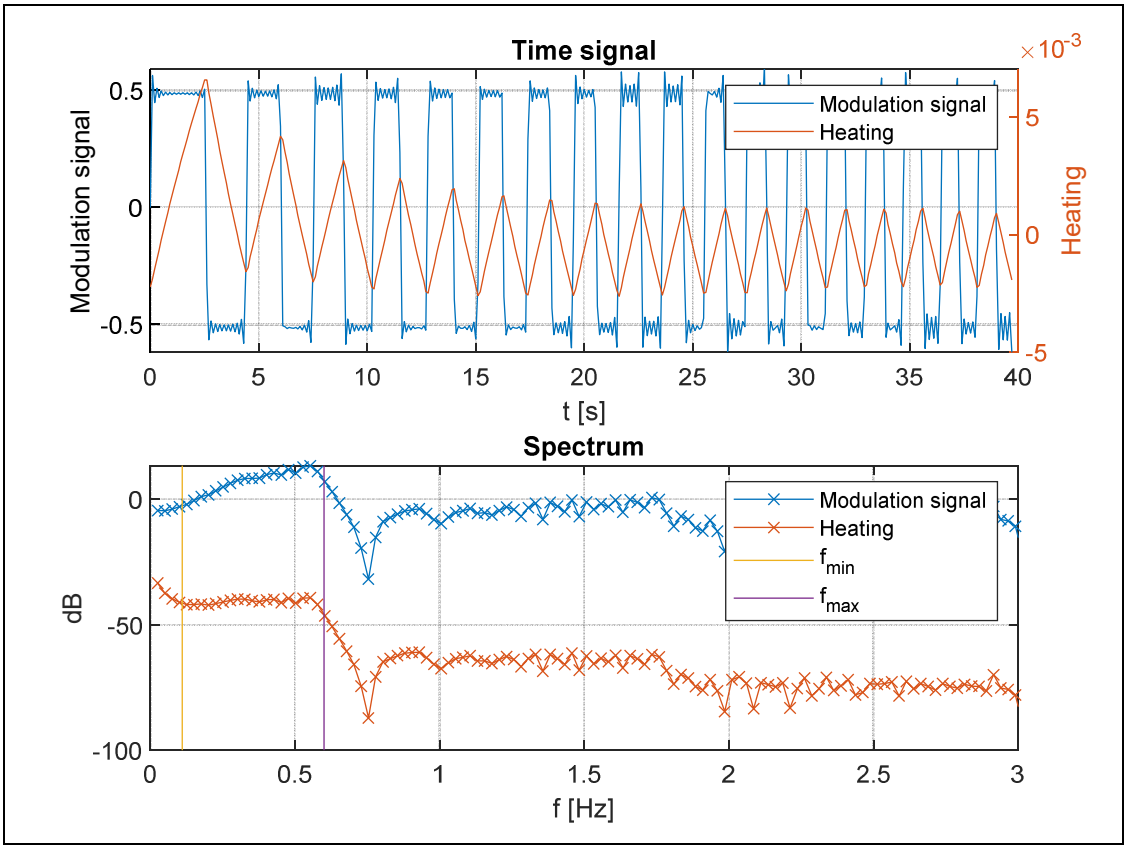

Figure 5. A square-wave cubic-root chirp with $f_0 \approx 0.1\ Hz$, $f_{max} \approx 0.6\ Hz$ and $T_m \approx 40\ s$. The heating signal spectrum is approximately flat in the modulation band. For $f < f_0$ the spectrum raises because of the neglected term $2h$ and imperfections in the chirp generation.

3.7. Interpretation

We now illustrate how the filtering is carried out by combining the results from the previous sections. Therefore, we refer to Figure 6 where the blue arrows indicate the physical signal flow leading to the temperature signal spectrum $T(f, f_x, f_y)$ which is the 3D Fourier transform (dashed green line) of $\tau(t, x, y)$. The plot of the spectrum T has a uniform extent in the direction of temporal frequencies since the modulation signal is a cubic-root chirp. Following the green arrows, $T(f, f_x, f_y)$ is multiplied with the radially symmetric filter $\mathrm{H}(f, f_r)$, then it is integrated over temporal frequencies (video to image conversion) such that we obtain the image spectrum $\hat{P}(f_x, f_y)$. The accompanying plot illustrates the dependencies described in equation (25). Eventually, by performing an inverse 2D Fourier transform, the image $\hat{p}(x, y)$ is obtained.

The filter $H(f, f_r)$ consists of two parts: a) the basic matched filter $\overline{G(f)M(f, f_r)}$, which assures maximal energy transfer for white noise and b) the correction term $\mathrm{K}(f, f_r)$ that balances between the frequency-depend signal-to-noise ratio (SNR), the propagation of the uncertainty over the heat transfer coefficient h and the optical transfer. By inspecting the plot of $K(f, f_r)$ we observe the

effects of α and σ_h: the former is the rate at which spatial frequencies, beyond the point where the noise power density dominates the signal power density, are attenuated; the latter creates an increase of $K(f, f_r)$ in regions of uncertainty with respect to h. The resulting "hill" of the correction term around the origin then causes a "dent" in the filter $H(f, f_r)$, which is ideally compensated by a bulge in higher temporal frequencies such that the optical transfer function can still be flat $\mathrm{OTF}(f_r) \approx 1$. This deformation can also be seen in the plot of the product of T and H (Figure 6).

In conclusion, we can say that a high σ_h removes perturbing thermal phenomena (strong heat convection and conduction causing high uncertainty over h) at the cost of increasing additive noise, whereas a strong α and a low f_{cut} suppress additive noise by smoothing the image.

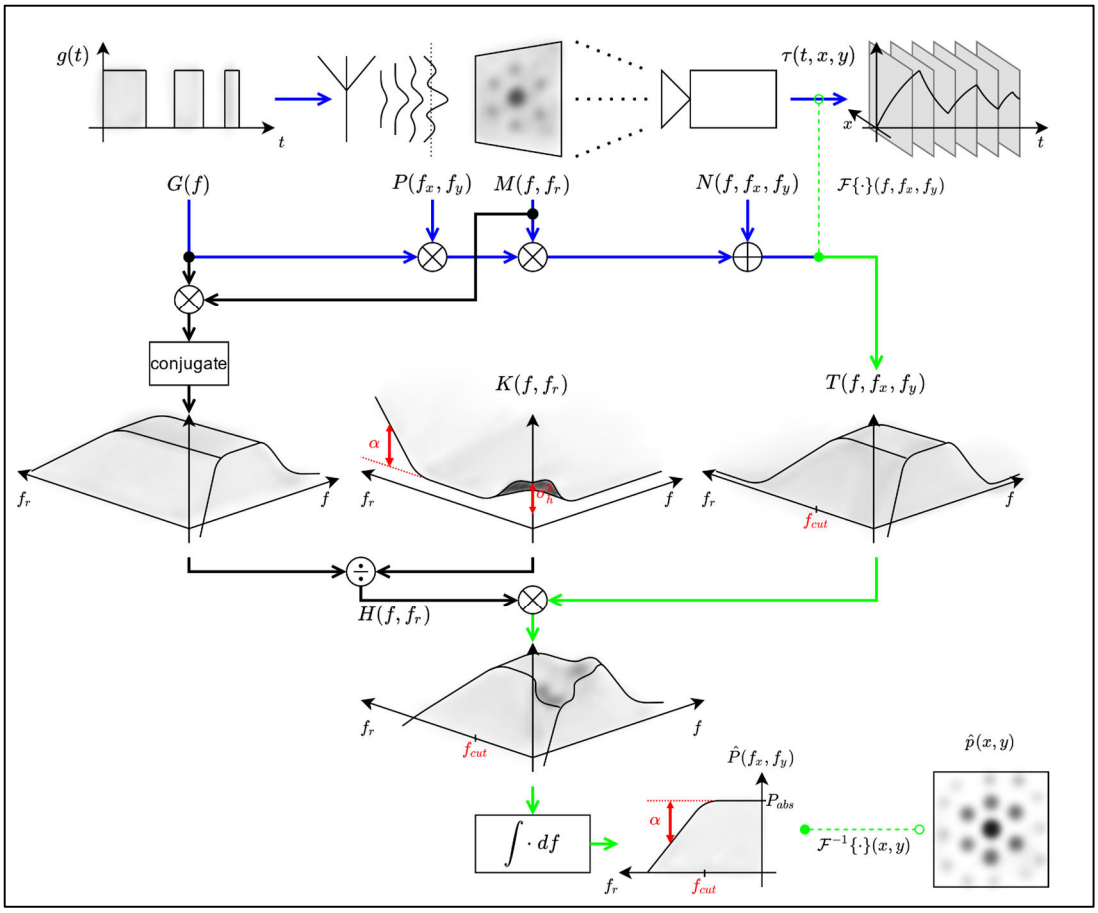

Figure 6. Illustration of the filtering process: the physical signal flow is depicted with blue arrows and the computed signal flow with green ones. Intermediate calculations are in black and user parameters are colored in red. The top row of symbols illustrates how the frames, i.e., the temperature signal $\tau(t, x, y)$, are obtained. In the Fourier domain, the radiated power distribution is multiplied by the film transfer function M and the camera noise N is added. The conjugate product of M and G provides the matched filter which is corrected by the K term and then applied to the T signal. After integration, the inverse Fourier transform provides the final image.

4. **Filtering results on the near field of an antenna**

4.1. Experimental set-up and results

To illustrate the effect of the proposed signal processing, we perform several measurements of a multiple-feed-per-beam antenna [17], whose electric near field exhibits a complex structure with different levels of intensity. The peripheral waveguides are connected to the central one by thin radial rectangular waveguides, which form coupling slots. Therefore, the intensity is decreasing from the central (powered) guide to the outside.

The film is placed at 5 mm from the source. We use a standard 50-mm lens to avoid large angle aberration as we place the camera at almost 1m. The images, therefore, correspond to a size (due to the lens field of view –FOV–) of about 10 x 10 cm^2. The source and the experimental set-up are shown in Figure 7:

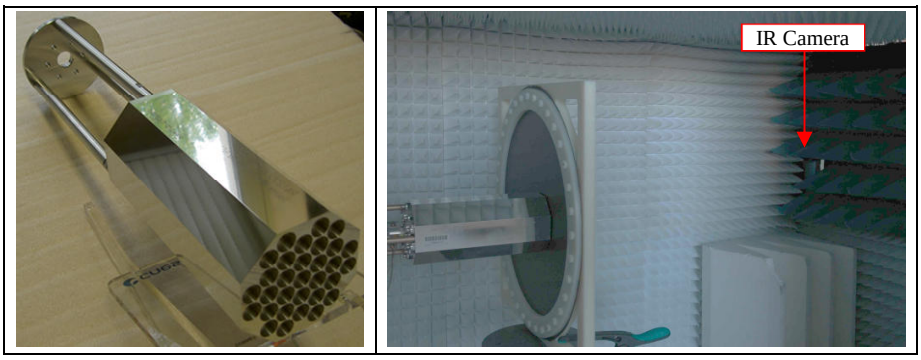

Figure 7. Multiple Feed per Beam radiating source; Set-up with source, film, and camera (located outside the anechoic chamber).

As shown in Figure 8 [18], lock-in thermography allows an accurate measurement that matches the numeric simulation. Here the incident power was $P_i = 3\ W$, (which leads to the highest signal without saturating the camera sensor).

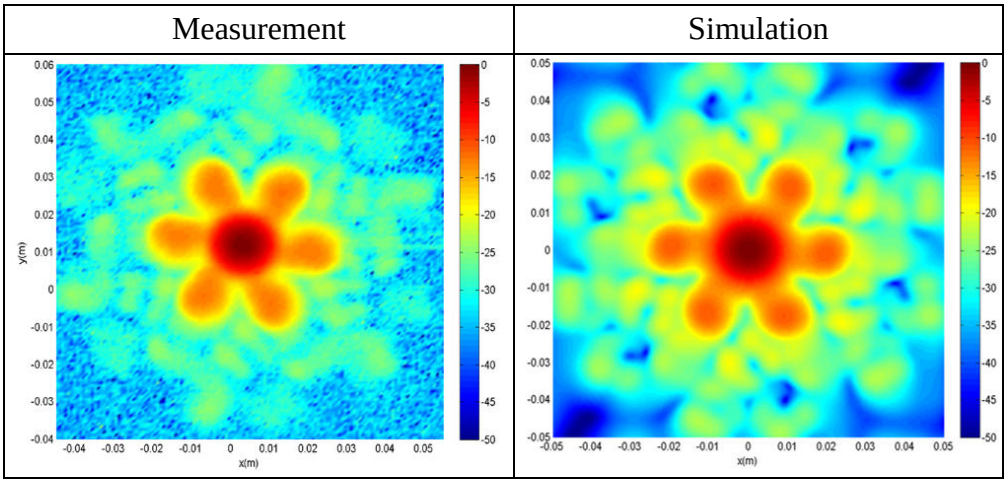

Figure 8. Power density map in the near-field zone: measurement vs. simulation.

To better illustrate the effect of the proposed signal processing, the incident power was chosen more than one order of magnitude lower ($P_i = 0.25\ W$). Conventionally, the only way of compensating a small signal power was by increasing the number of frames since the noise power is inversely proportional to the number of frames (which is equivalent to a decrease of 5 dB per decade in EM power density). This can be achieved by increasing either the sampling rate (FPS) or the acquisition time (see yellow line in Figure 10). However, the filtering approach is more efficient as it is illustrated in the next paragraph.

4.2. Square modulation

We apply a square modulation at a frequency of $0.3\ Hz$, which is somewhat an arbitrary choice as mentioned in section 3.6. However, our experience shows that a modulation frequency between 0.1 and $1\ Hz$ yields acceptable results for the given antenna. Before beginning the acquisition, we wait about 30 seconds to avoid the transient thermal state. Then, we determine $h_0 = 15\ \mathrm{W}m^{-2}$, $\alpha = 8$ and $\mathrm{f_{cut}} = 40\ \mathrm{m}^{-1}$ by inspection of the average temperature spectrum, and that $P_{abs} \approx 60\ mW$ (close to 20% of the incident power ($P_i \approx 250\ mW$), as expected.

The demodulated image, as well as a horizontal and a vertical slice, are given for different filtering approaches in Figure 9. Qualitatively, we observe that the contrast of the images a) to d) as well as that of the slices improves with increasing filtering complexity. The conventional approach (Figure 9.a) and the in-phase demodulation (Figure 9.b) exhibit the expected difference of $1.5\ dB$ (which is half of the $3\ dB$ stated in section 3.1 where we were referring to the signal power, i.e., the squared EM power). The matched filter (Figure 9.c) adds $6\ dB$ and the Wiener filter (Figure 9.d) another $1\ dB$ of dynamics. The last two reveal details below $-20dB$ in the (green) horizontal slice.

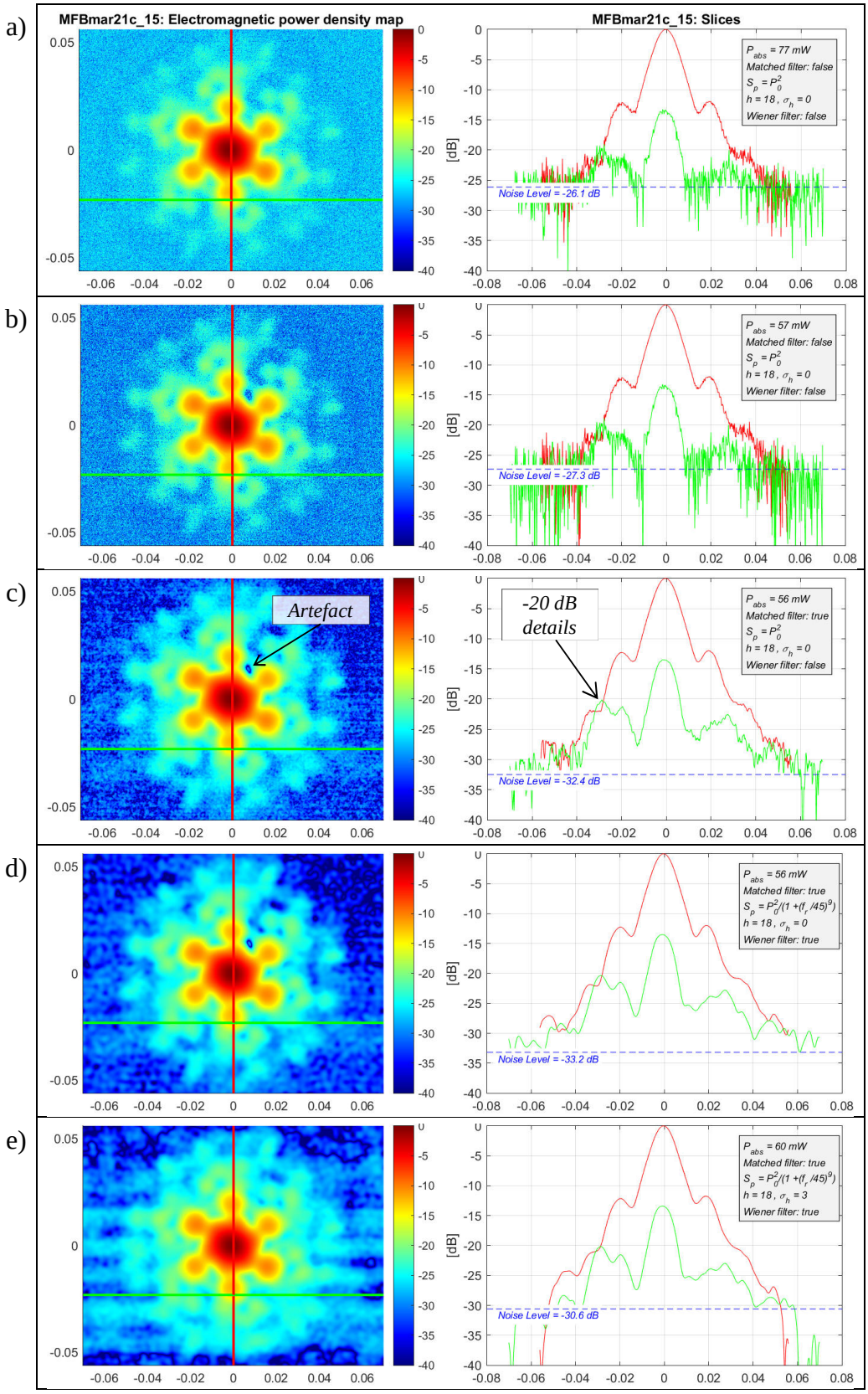

Figure 9. Power density, vertical (red) and horizontal (green) slices: a) Conventional approach (no filter), b) In-phase demodulation (no filter), c) Matched filter -local maxima at -20 and -22 dB appear, d) Wiener filter, e) Wiener filter with $\sigma_h > 0$.

Throughout Figure 9b) to d), we can observe a dark spot at $x = 0.01m$ and $y = 0.01\,m$, which is not part of the radiation pattern of the antenna. Considering an uncertainty over the heat transfer coefficient h during the filtering, i.e., $\sigma_h > 0$, we can partially remove this thermal artefact. However, this comes at the cost of increasing the noise floor of the image as it can be seen in Figure 9e).

Below, we present the noise levels (measured by the mean-squared signal over 10,000 pixels in areas of the image where no signal from the antenna is expected) as a function of the number of images recorded, for the different filters. Figure 10 exhibits approximately the expected trend of -5 dB per decade, but also shows that more than 8 dB can be gained by using a matched or Wiener filter.

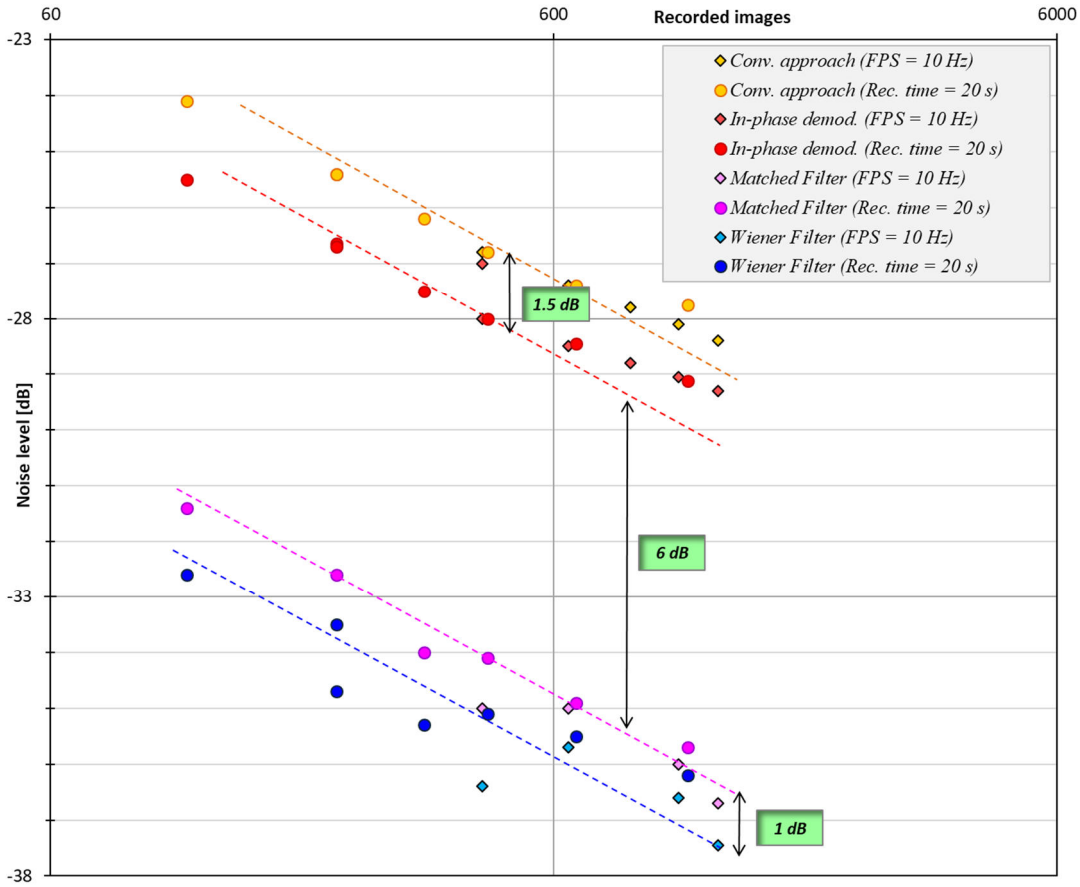

Figure 10. Noise level as a function of the number of images for different filtering approaches (the dotted lines have the theoretical slope of -5 dB per decade).

4.3. Chirp modulation

It has been shown that the proposed signal processing improves the image dynamics. We now show how the usage of a chirp can efficiently deal with the trade-off between thermal artefacts and noise-floor level. We, therefore, apply the same square-wave cubic-root chirp as in section 3.6. Figure 11 depicts the demodulated images for four different values of σ_h. As we have seen in Figure 5, the signal spectrum contains energy below f_0, we, thus, expect strong thermal artefacts if we do not include

considerations about the uncertainty over h in the filtering. Indeed, the image with $\sigma_h = 0$ is tainted with "big stains". When increasing σ_h these effects disappear. However, at $\sigma_h = 1.5$ the noise floor is becoming disturbing, which is caused by the filter suppressing too much signal energy in the low temporal frequency range. For this acquisition, best results are obtained with $\sigma_h \approx 0.6$.

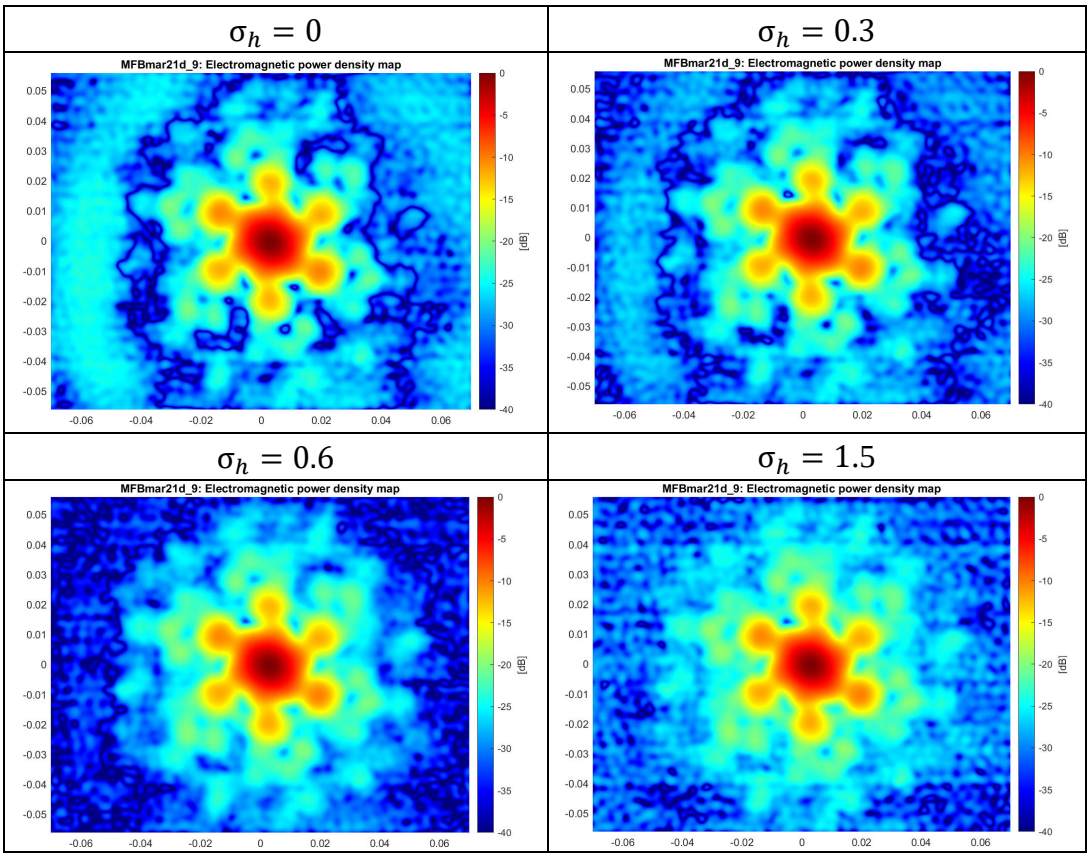

Figure 11. Square-wave cubic-root ($T_m = 39.8\ s$, $f_0 = 0.1\ Hz$ and $f_{max} = 0.6\ Hz$) with four different values of σ_h (from 0 to a relatively high value of 1.5).

Finally, we compare the performance of this chirp with those of a square wave at the edges of the modulation band (f_0 and f_{max}). In Figure 12, we can see that the image at $f_0 = 0.1\ Hz$ strongly exhibits artefacts as well as some light but large "stains". At the other end of the band, $f_{max} = 0.6$Hz, no thermal artefacts are apparent. However, the noise level is higher than the one at f_0. The image of the chirp does not exhibit thermal artefacts and the noise level is lower than at $f_{max} = 0.6$Hz. This shows that the usage of a chirp allows an efficient balancing of the spectral components such that the image is free of artefacts and that a good SNR is sustained.

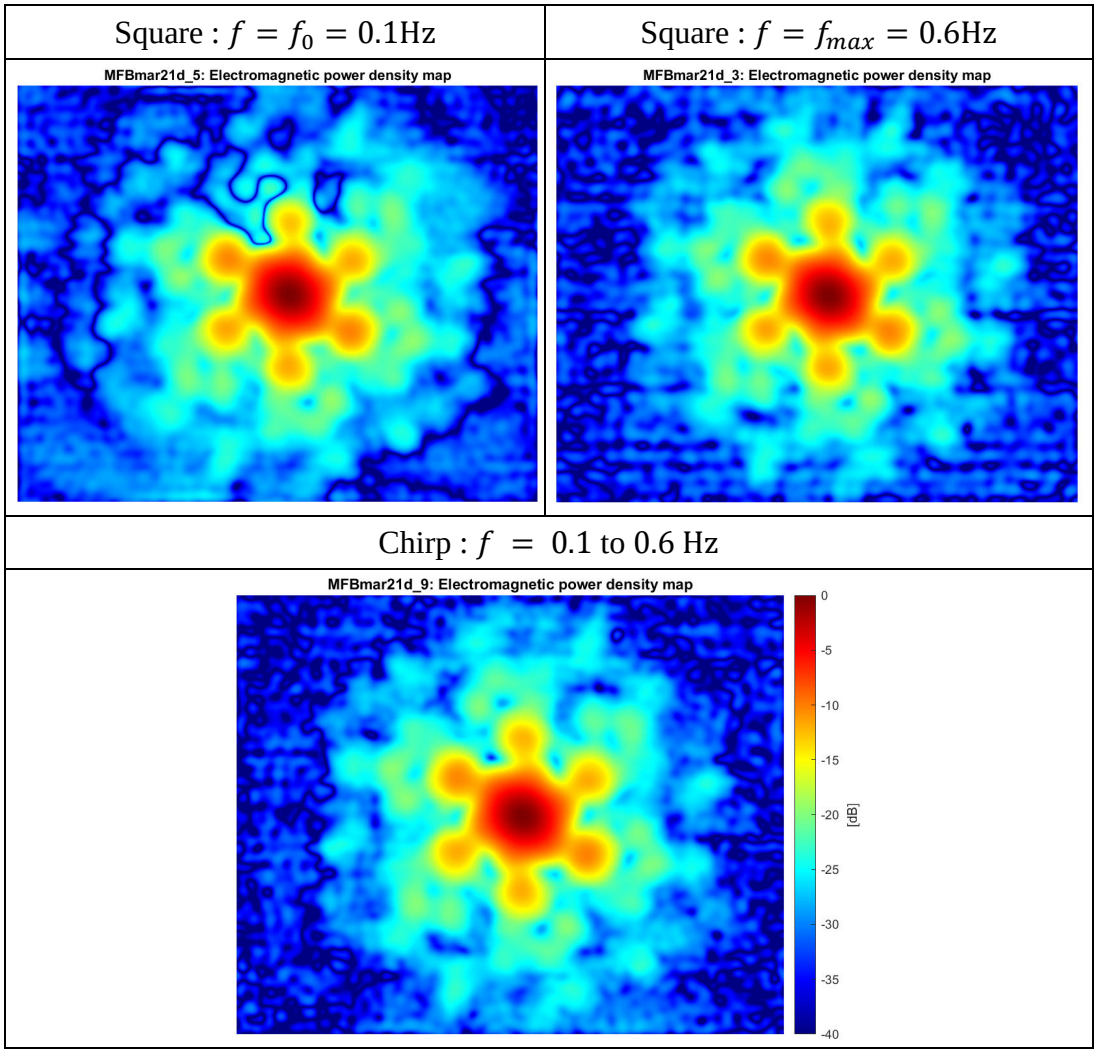

Figure 12. Images modulated with a square wave at $f = f_0 = 0.1\ Hz$ and $f = f_{max} = 0.6\ Hz$, and with a square-wave cubic-root chirp.

5. Conclusion

The advantage of the EMIR method over scanning probe-based field mapping techniques is its short acquisition time and its subwavelength resolution. In contrast to analogue buffered locked-in thermography systems, digital thermal cameras make the entire thermal video signal accessible. This enables the use of DSP to further extend the advantages of the method. By modelling the entire measurement system as an imaging system, we can optimize the signal processing and the modulation signal as a function of the sensing film properties. Beyond a traditional matched and a Wiener filtering approach, we established a filter that efficiently deals with the trade-off between SNR (image dynamic), uncertainty over system parameters (image artefacts) and optical transfer (image resolution). Further, we demonstrate how we can use the frequency versatility of a chirp modulation signal to fully exploit the potential of the proposed filter. The achieved gain allows a significant reduction of the recording time and/or the frame rate and can contribute to better characterize the EM field of radiating sources in a wide range of frequencies. Finally, it should be noted that the described methods can also be applied in the neighboring context of fluorescence thermography of the electromagnetic field [19].

Acknowledgments

The authors thank the Centre National d'Études Spatiales (French Space Agency) for providing the multiple-feed-per-beam antenna for testing and for the near-field simulation results.

References

[1] J.D. Norgard et al., "Infrared measurements of electromagnetic fields", *QIRT 92*, Editions Europ. Therm. et Industrie, Paris, France, 1992, pp. 308-312.

[2] D. Balageas, P. Levesque, A. Déom, "Characterization of electromagnetic fields using lock-in IR thermography", *Thermosense* XV, SPIE 1993. https://doi.org/10.1117/12.141978.

[3] P. Levesque, L. Leylekian, "Electromagnetic Field Sensor By Infrared Thermography", *French Patent* n°FR2787583B1, 1998.

[4] https://www.telops.com/products/high-speed-cameras/lwir-cameras.

[5] D. Balageas, P. Levesque, "EMIR: a photothermal tool for electromagnetic phenomena characterization", *Revue générale de thermique* 1998;37(6). https://doi.org/10.1016/S0035-3159(98)80050-0.

[6] J.W. Goodman, “Introduction to Fourier Optics”, *3rd Revised ed. Roberts & Company*; 2016. ISBN10 0974707724.

[7] M.N. Özisik, “Heat Conduction”, *J. Wiley & Sons*, Raleigh, North Carolina; 1993.

[8] R. Byron Bird, Warren E. Stewart, Edwin N. Lightfoot, “Transport Phenomena”. *John Wiley and Sons*, 1960.

[9] A.C. Offord, “On Hankel transforms”, *Proceedings of the London Mathematical Society*, 1935;39(2):49–67.

[10] O. Breitenstein, M. Langenkamp, “Lock-in Thermography : Basics and Use for Functional Diagnostics of Electronic Components”, *Springer Series in Advanced Microelectronics*, Springer, Berlin and Heidelberg; 2003.

[11] M. Najim, “Modeling, Estimation, and Optimal Filtering in Signal Processing”, *J. Wiley & Sons*, 2010; 105-147.

[12] M. Najim, “Matched and Wiener Filters”, *John Wiley & Sons*; 2010;3:105-147.

[13] D. Prost, F. Issac, P. Reulet, “Large scale measurement of microwave electric field using infrared thermography and electromagnetic simulation”, *Progress in Electromagnetics Research Symposium*, PIERS 2011.

[14] A. Torralba, A. Oliva, “Statistics of natural image categories”, *Network: Computation in Neural Systems*, 2003;14 (3). https://doi.org/10.1088/0954-898X_14_3_302.

[15] S. Laureti, S. Sfarra, H. Malekmohammadi, P. Burrascano, D.A. Hutchins, L. Senni, G. Silipigni, X. Maldague, M. Ricci, “The use of pulse-compression thermography for detecting defects in paintings”, *NDT & E International*, 2018;98:147–154. https://doi.org/10.1016/j.ndteint.2018.05.003.

[16] D.P. Almond, S.L. Angioni, S.G. Pickering, “Long pulse excitation thermographic non-destructive evaluation”, *NTD&E International*, 2017, 87. https://doi.org/10.1016/j.ndteint.2017.01.003.

[17] C. Leclerc, M. Romier, H. Aubert, A. Annabi, “Ka-Band Multiple Feed per Beam Focal Array Using Interleaved Couplers”, *IEEE Trans. Microwave Theory and Techniques*, 2014;62(6). doi: 10.1109/TMTT.2014.2320697.

[18] D. Prost, F. Issac, M. Romier, D. Belot, “EMIR Field Imaging for Diagnosis and Characterization of Space Antennas”, *38th ESA Antenna Workshop*, ESTEC Noordwijk. 2017.

[19] S. Faure, J.F. Bobo, D. Prost, F. Issac, J. Carrey, “Electromagnetic field intensity imaging by thermofluorescence in the visible range”, *Phys. Rev. A, Gen. Phys. Appl.* 2019, 11(5). https://doi.org/10.1103/PhysRevApplied.11.054024.